Chapter 6
High-Bandgap Silicon Nanocrystal Solar Cells: Device Fabrication, Characterization, and Modeling

Philipp Löper, Mariaconcetta Canino, Manuel Schnabel, Caterina Summonte, Stefan Janz, and Margit Zacharias

Abstract Silicon nanocrystals (Si NCs) embedded in Si-based dielectrics provide a Si-based high-bandgap material (1.7 eV) and enable the construction of crystalline Si tandem solar cells. This chapter focusses on Si NC embedded in silicon carbide, because silicon carbide offers electrical conduction through the matrix material. The material development is reviewed, and optical modeling is introduced as a powerful method to monitor the four material components, amorphous and crystalline silicon as well as amorphous and crystalline silicon carbide. In the second part of this chapter, recent device developments for the photovoltaic characterization of Si NCs are examined. The controlled growth of Si NCs involves high-temperature annealing which deteriorates the properties of any previously established selective contacts. A membrane-based device is presented to overcome these limitations. In this approach, the formation of both selective contacts is carried out after high-temperature annealing and is therefore not affected by the latter. We examine p-i-n solar cells with an intrinsic region made of Si NCs embedded in silicon carbide. Device failure due to damaged insulation layers is analyzed by light beam-induced current measurements. An optical model of the device is presented for improving the cell current. A characterization scheme for Si NC p-i-n solar cells is presented which aims at determining the fundamental transport and recombination properties, i.e., the effective mobility lifetime product,

P. Löper (✉) • M. Schnabel • S. Janz
Fraunhofer ISE, Heidenhofstr. 2, 79110 Freiburg, Germany
e-mail: philipp.loeper@ise.fraunhofer.de; manuel.schnabel@ise.fraunhofer.de;
stefan.janz@ise.fraunhofer.de

M. Canino • C. Summonte
CNR-IMM, Via Piero Gobetti 101, 40129 Bologna, Italy
e-mail: canino@bo.imm.cnr.it; summonte@bo.imm.cnr.it

M. Zacharias
IMTEK, University Freiburg, Georges-Koehler-Allee 103, 79110 Freiburg, Germany
e-mail: zacharias@imtek.uni-freiburg.de

of the nanocrystal layer at device level. For this means, an illumination-dependent analysis of Si NC p-i-n solar cells is carried out within the framework of the constant field approximation. The analysis builds on an optical device model, which is used to assess the photogenerated current in each of the device layers. Illumination-dependent current–voltage curves are modelled with a voltage-dependent current collection function with only two free parameters, and excellent agreement is found between theory and experiment. An effective mobility lifetime product of 10^{-10} cm^2/V is derived and confirmed independently from an alternative method. The procedure discussed in this chapter is proposed as a characterization scheme for further material development, providing an optimization parameter (the effective mobility lifetime product) relevant for the photovoltaic performance of Si NC films.

1   Crystalline Si Tandem Solar Cells

The impressive success in reaching very high conversion efficiencies with c-Si [1] has triggered the search for novel concepts overcoming the fundamental efficiency limits. Module costs have been reduced significantly due to upscaled production, but an ongoing long-term cost reduction cannot be achieved only with upscaled production and ever more sophisticated equipment. Rather, new solar cell concepts are required that permit overcoming the physical limitations of today's technologies. Figure 6.1 depicts the AM1.5G solar spectrum and illustrates the energy that can theoretically be converted by a silicon solar cell.

The theoretical efficiency limit arises from two loss mechanisms. Photons with energy less than the bandgap energy are not absorbed by the solar cell (red and rightmost arrow in Fig. 6.1), giving rise to transmission losses. High-energy photons, on the other hand, create a high-energy electron–hole pair in the solar
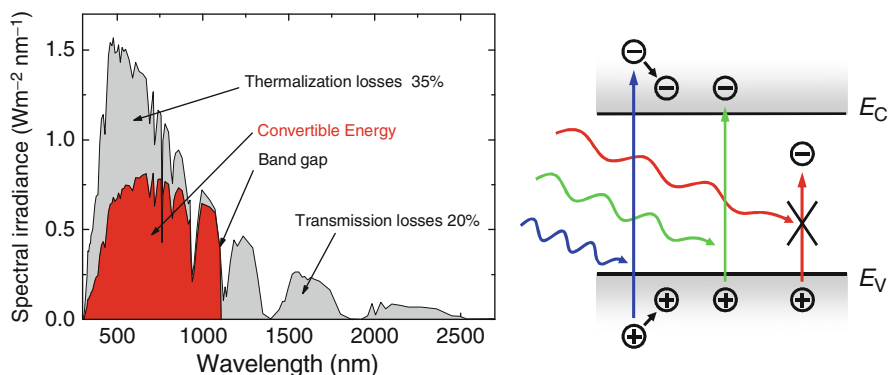

Fig. 6.1 (*Left*) The AM1.5G solar spectrum and the maximum energy convertible to electricity by a silicon solar cell. The fundamental efficiency limit arises from the loss mechanisms shown on *right*. The figure was taken from [2]
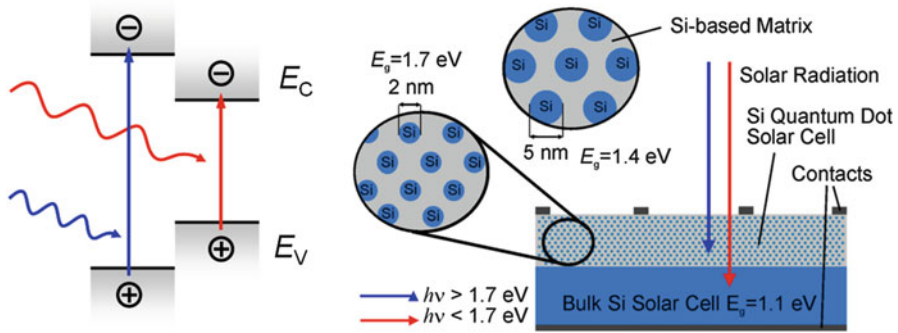
Fig. 6.2 (*Left*) Principle of stacked absorbers, each of which is matched to one wavelength. (*Right*) Scheme of an all-crystalline silicon tandem solar cell. The *top* solar cell consists of Si nanocrystal quantum dots that absorb only the high-energy photons. The bandgap of the Si nanocrystal quantum dots can be tuned by controlling the crystal size. The figure was taken from [2]

cell (blue and leftmost arrow in Fig. 6.1). The excess energy is dissipated to the crystal lattice (thermalization), and only a fraction of the incident solar radiation energy is converted to electricity. Ideal energy conversion is possible only for photons whose energy just matches the bandgap energy, indicated by the green arrows in Fig. 6.1.

The conversion of electromagnetic radiation to electrical energy can be optimized by matching the solar cell to the incident spectrum. This can be achieved by stacking multiple solar cells, each of which is adapted to a certain spectral region. Figure 6.2 (left) depicts the principle of such a multijunction or tandem solar cell. Each sub-cell absorbs only a certain spectral region and is optimized to minimize the thermalization upon illumination with this part of the solar spectrum. Tandem solar cells are already commercially available, and efficiencies of 37.7 % have been reached with III–V materials [3]. However, III–V solar cells are only of limited use for large-area power generation as several of the elements involved are toxic, rare, and expensive. The strong motivation to stick to silicon (Si) arises from the fact that it is the second most abundant element in the earth's crust [2], that it is not toxic, that it is quite strong mechanically, and that solar cell manufacturers can build on the highly developed Si microelectronics technology. Therefore, advanced solar cell concepts are desirable that are based on Si materials and compatible with Si technology. Tandem solar cells have been realized with amorphous and micro-crystalline Si with a record efficiency of 13.4 %. However, amorphous and micro-crystalline Si solar cells suffer from the so-called Staebler–Wronski effect [4], which reduces the efficiency by up to 30 % during operation.

A material which consists of crystalline Si and features a high bandgap is provided by silicon nanocrystals (Si NCs) embedded in a Si-based matrix material.

Since the first observation of visible photoluminescence from anodically etched Si [5], nanostructured Si has received a lot of attention due to the promise of a
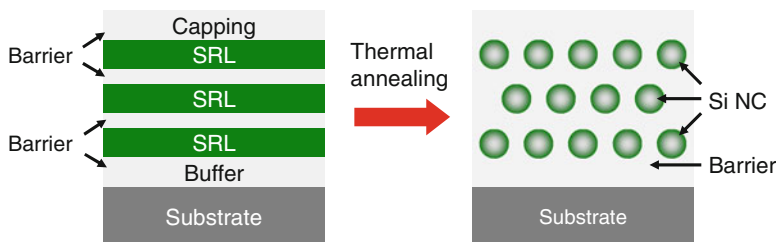
Fig. 6.3 Scheme for the fabrication of a Si nanocrystal superlattice by the multilayer approach [6]. Silicon-rich layers (SRL) are sandwiched between stoichiometric layers (barrier). The barrier layers restrict the Si NC growth and thereby enable a narrow size distribution. Si NC formation is induced by thermal annealing at high temperatures, usually around 1,100 °C. The figure was taken from [2]

high-bandgap material compatible with Si technology. In this context, a "high bandgap" refers to a bandgap value higher than in the extended Si crystal (bulk).

The bandgap has since been shown to be well controllable by tuning the NC size and thus the quantum confinement. The principle of a crystalline Si tandem solar cell is sketched in Fig. 6.2 (right). The high-energy photons (blue arrow) are absorbed in the Si NC top solar cell, while photons with less energy are transmitted by the latter and absorbed in the bottom solar cell. The bottom solar cell is made of bulk Si, e.g., a Si wafer or a thin film crystalline Si.

For large-area fabrication of size-controlled Si NCs, amorphous multilayer precursors are deposited and then thermally annealed to form the Si NCs [6]. The multilayer consists of a stack of alternating Si-rich (SRL) and stoichiometric (barrier) layers of a Si compound as shown in Fig. 6.3. Upon annealing, the Si excess in the Si-rich layers precipitates and clusters. Subsequently, the clusters are solid phase crystallized at temperatures around 1,100 °C. The stoichiometric layers act as barriers towards crystallite growth and thus limit the Si NC size.

2 Membrane-Based p-i-n Device for Substrate-Free Characterization

The necessity of using temperatures of around 1,100 °C for the fabrication of the Si NC layer imposes severe requirements on the thermal stability and the expansion coefficient of the substrate. Device fabrication is further complicated because the substrate hinders the access to the rear side of the Si NC layer. The simplest method is to use a conductive substrate as a back contact, e.g., a Si wafer. However, this complicates device analysis because both the Si NC layer as well as the Si wafer substrate, which even on its own would make a good solar cell, can contribute to the measured current–voltage (*IV*) curve. The Si NC layer contribution to the *IV* curve can theoretically be distinguished from that of the wafer using monochromatic light with a penetration depth below the Si NC layer thickness. The penetration depth $1/\alpha$
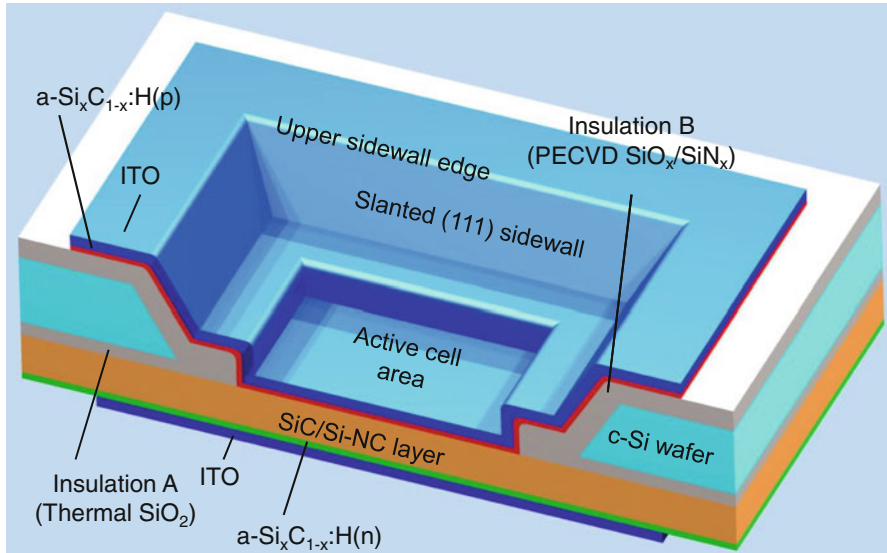
Fig. 6.4 Sketch of the membrane-based device. Reprinted with permission from [7]

for Si NCs in SiO_2 is about 10 μm at 3 eV photon energy and 1 μm at 4 eV photon energy [5]. Technologically viable Si NC layers are usually thinner than 300 nm. As the vast majority of the solar spectrum comprises photons with energies below 4 eV a large fraction of the incident light is thus transmitted through the Si NC film and generates charge carriers in the substrate wafer. This impedes the distinction between the Si NC contribution and that of the substrate wafer to the measured *IV* curve. A solution could be the choice of a substrate wafer with an optical bandgap higher than that of the Si NC film, e.g., a silicon carbide wafer or an epitaxial gallium nitride on a silicon carbide or a sapphire wafer. However, the substrate wafer is also required to have a suitable work function and electron affinity to work as an electron or a hole collector. The terms "electron collector" and "hole collector" are used hereinafter according to [6] to describe the part of the solar cell that collects (contacts) the respective charge carrier type. They are frequently also called "emitters," "back surface field," or "selective contacts" in the literature.

In all concepts that involve a substrate which is also used as the back contact, the physical properties of the electrical back contact cannot be tuned independently from the solid-phase crystallization process of the Si NC layer. Any change of the thermal annealing step will also affect the properties of the electrical contact. A detailed review of Si NC devices that have been realized so far can be found in [7].

To enable an unequivocal photovoltaic characterization of Si NC films without the flaws discussed above, a membrane-based device was developed as shown in Fig. 6.4 [8]. Its key feature is the local removal and then encapsulation of the substrate after solid-phase crystallization of the Si NCs. After encapsulation of the
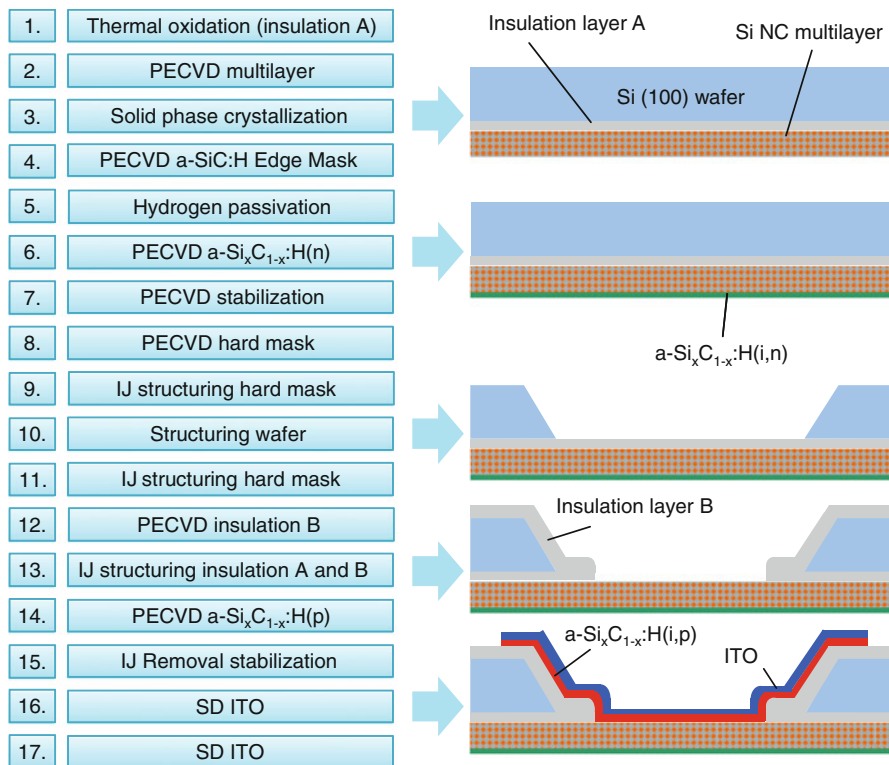
1.	Thermal oxidation (insulation A)
2.	PECVD multilayer
3.	Solid phase crystallization
4.	PECVD a-SiC:H Edge Mask
5.	Hydrogen passivation
6.	PECVD a-Si$_x$C$_{1-x}$:H(n)
7.	PECVD stabilization
8.	PECVD hard mask
9.	IJ structuring hard mask
10.	Structuring wafer
11.	IJ structuring hard mask
12.	PECVD insulation B
13.	IJ structuring insulation A and B
14.	PECVD a-Si$_x$C$_{1-x}$:H(p)
15.	IJ Removal stabilization
16.	SD ITO
17.	SD ITO

Fig. 6.5 (*Left*) Flow chart of the cell process for membrane-based p-i-n devices with a SiC-based absorber and doped Si$_x$C$_{1-x}$:H as electron and hole collectors. Plasma-enhanced chemical vapor deposition (PECVD), sputter deposition (SD), inkjet printing (IJ), and wet chemical etching are used for deposition and structuring. (*Right*) The resulting structure is indicated after specific process steps. The front side is facing down in this sketch. The figure was taken from [2]

substrate to insulate it electrically and the subsequent local opening of the encapsulation at the Si NC layer, the Si NC layer can be accessed freely from both sides. A Si wafer is used as a substrate, and insulation and structuring are realized with Si-based dielectric layers deposited by PECVD. The membrane-based device structure shown in Fig. 6.4 permits a free choice of the selective contact material and the interface pretreatment. All electrically active materials can be chosen to have a bandgap comparable to or higher than the Si NC film. This permits an unambiguous characterization of the Si NC material. The structure can be realized as a p-i-n diode using an intrinsic and thin Si NC absorber. Photocurrent collection is thus enhanced by the electrical field between the hole collector (p) and the electron collector (n). Furthermore, device fabrication is compatible with standard Si process technology.

The fabrication sequence for a membrane device with an absorber that consists of Si NCs embedded in SiC is shown in Fig 6.5. The SiC/Si$_x$C$_{1-x}$ multilayer is deposited on a thermally oxidized wafer and then annealed at temperatures up to

1,100 °C to form the Si NCs [9]. The wafer is removed locally and insulated from the Si NC film by means of dielectric layers. After structuring the insulation layers, electron and hole collectors are formed by n-type and p-type a-Si$_x$C$_{1-x}$:H, respectively, and indium tin oxide (ITO) is deposited as a transparent contact on both sides. Details on the fabrication process can be found in [8] and [9]. All structuring steps except the local removal of the substrate are performed by inkjet printing of a hotmelt wax and etching in hydrofluoric acid (HF).

As the electron and hole collectors are established after the formation of the Si NCs by solid-phase crystallization, their electronic properties are not affected by the latter. The membrane-based device is thus a viable test device for the characterization of the physical properties of Si NC films prepared by high-temperature thermal annealing.

3 Silicon Nanocrystals in SiC by Solid-Phase Crystallization

Si NCs embedded in a SiC matrix are manufactured by depositing alternating Si-rich carbide (SRC) and SiC layers according to the multilayer approach described in Sect. 1. This method has the advantage of allowing the desired Si NC size and density in the plane to be tuned independently via the SRL thickness and the Si excess in the SRL, respectively. The structure resulting from this method can be considered as a Si NC superlattice. The method proved to be effective for producing Si NC superlattices in SiO$_2$ [10]. In analogy to the case of SiO$_2$, the manufacturing of Si NCs in SiC requires the calibration of the processing conditions as a function of the desired Si NC density in the plane. This section gives an overview of the manufacturing technology and related issues as well as of the structural and light absorption properties of the resulting material.

3.1 Deposition by PECVD

The SiC and SRC layers can be deposited by sputtering [11] or by plasma-based techniques, such as inductively coupled plasma (ICP) [12] and PECVD [13–15].

The material described in the following is produced by PECVD. This technique involves dissociating the molecules of the Si, C, and H containing gas precursors by a glow discharge to produce a plasma. Generally the employed gases are SiH$_4$, CH$_4$, and if necessary H$_2$ [14] or Ar [13] for dilution. Monomethylsilane (MMS) has also been used as a Si and C precursor; the combination of MMS and SiH$_4$ allows for the control of the Si and C contents [15]. Since the dissociation is assisted by a physical mechanism, the deposition on the substrate is achieved at much lower temperatures than by chemical vapor deposition (CVD). In order to achieve sufficiently low

growth rates to produce SRC and SiC layers only a few nm thick, the plasma power density that can be used is limited. This in turn means that not all precursor molecules are fully dissociated by the plasma. Many are incorporated into the film as molecular radicals, and as all precursor gas molecules contain hydrogen, this implies a high incorporation of H. The substrate temperature being lower in PECVD than in CVD, the in situ H effusion is limited, which results in a large H content in PECVD layers. The large hydrogen content is the main feature that characterizes PECVD material also with respect to sputtered films. The Si content in the SRC as the parameter that determines the Si NC density in the SRC layer [10] is tuned by varying the SiH_4 and CH_4 flow rates.

In device manufacturing, the knowledge of the volume fractions can be used both as a check of the phase separation achieved [16] and as a tool to vary the optical properties of the solar cell absorber, because in composite materials the optical properties are directly related to the volume fraction of the components.

The design of a Si NC device also requires the knowledge of the material transformations in response to the thermal treatments. Upon annealing the materials crystallize and lose hydrogen, eventually reaching the density of bulk Si or SiC. This implies that the deposited layers undergo a shrinkage that has to be taken into account in device design [17].

Equations (6.1) and (6.2) describe the relationships between the atomic composition in as-deposited materials and the volumes of the components after annealing [17].

The volume of the Si excess in a multilayer is calculated by weighting the Si-rich carbide volume by the volume of the Si excess in the Si-rich carbide:
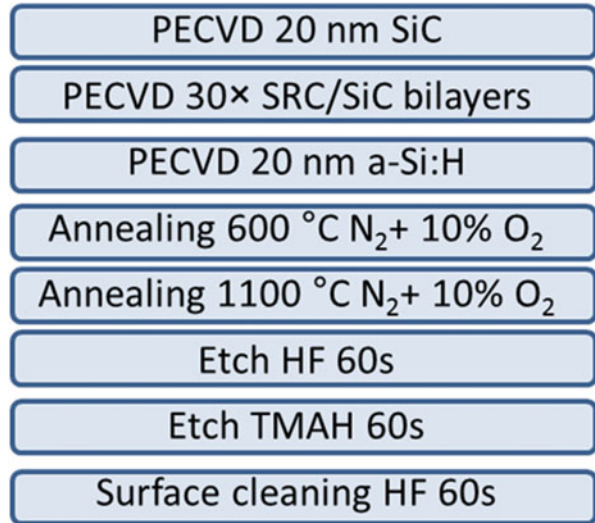
$$V_{Si} = V_{Si,SRC} \cdot \frac{d_{SRC}}{d_{SRC} + d_{SiC}}. \tag{6.1}$$

V_{Si} is the volume of the Si excess in the multilayer, d_{SiC} and d_{SRC} the thicknesses of the annealed SiC and the SRC, respectively, and $V_{Si,SRC}$ the volume of the Si excess in the annealed SRC.

The volume of the Si excess in an SRC layer after phase separation, $V_{Si,SRC}$, depends on the Si fraction x according to a general formula for silicon alloys, such as Si-rich oxide, SRC, and Si-rich nitride. In the case of an SRC the volume fractions occupied by the Si and SiC phases under the hypothesis of complete separation are

$$
\begin{aligned}
V_{Si} &= \frac{(2x-1) \cdot m_{Si} \cdot \rho_{SiC}}{(1-x) \cdot (m_{Si} + m_C) \cdot \rho_{Si} + (2x-1) \cdot m_{Si} \cdot \rho_{SiC}} \\
V_{SiC} &= \frac{(1-x) \cdot (m_{Si} + m_C) \cdot \rho_{Si}}{(1-x) \cdot (m_{Si} + m_C) \cdot \rho_{Si} + (2x-1) \cdot m_{Si} \cdot \rho_{SiC}}
\end{aligned}. \tag{6.2}
$$

Fig. 6.6 Sequence of the fabrication steps optimized to produce Si NCs in SiC

| PECVD 20 nm SiC |
| PECVD 30× SRC/SiC bilayers |
| PECVD 20 nm a-Si:H |
| Annealing 600 °C N₂+ 10% O₂ |
| Annealing 1100 °C N₂+ 10% O₂ |
| Etch HF 60s |
| Etch TMAH 60s |
| Surface cleaning HF 60s |

x is the Si content in the SRC, which means that $(2x - 1)$ is the excess of Si atoms and $(1 - x)$ the C content, m_{Si} and m_C are the atomic weights of the Si and C atoms, respectively, and ρ_{Si} and ρ_{SiC} are the densities of the Si and SiC components after annealing.

Furthermore, appropriate design of a multilayer requires the insertion of a crystallization barrier between the Si substrate and the multilayer in order to prevent the Si substrate from acting as crystallization seed during the subsequent annealing. Such a layer can reasonably be amorphous SiC or SiO₂.

In the case of a SiC matrix, an encapsulation is needed to prevent SiC reacting with oxygen during annealing, as this would lead to an undesired surface oxidation [18, 19]. Amorphous silicon has been found to be a suitable encapsulation layer as it can be deposited in the same PECVD chamber from similar gas precursors as the multilayer and oxidizes instead of the multilayer on annealing. Addition of 10 % O₂ to the nitrogen normally used as an annealing ambient helps to make the oxidation of the encapsulation more reproducible. The resulting SiO₂ and the residual μc-Si encapsulation are removed by wet etching. The process sequence is summarized in Fig. 6.6. This procedure results in a SiC-rich surface [19].

In the following sections, the multilayers will be labeled with a sequence of three numbers, representing the as-deposited multilayer layout: the first number represents the Si content x in the SRC multiplied by 100, the second the as-deposited SRC thickness in nm, and the third the integer part of the as-deposited SiC thickness in nm. For example, 65-3-5 is a multilayer in which the Si fraction in the SRC layer is 0.65, and the thickness of the SRC and the SiC is 3 and 5 nm, respectively. The number of bilayers is 30 in all cases.
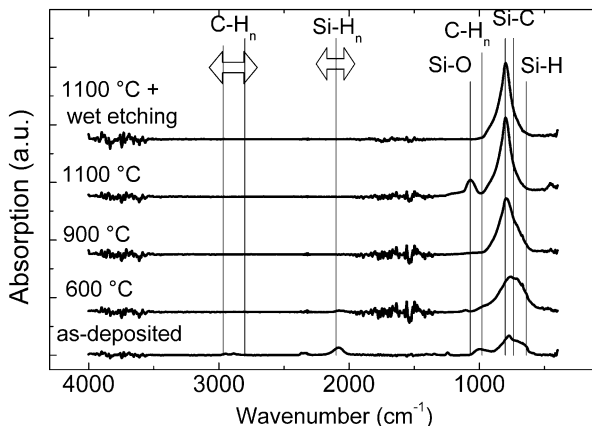
Fig. 6.7 Mid infrared absorption spectra of 65-3-3 after different fabrication steps: as-deposited, after annealing at 600 °C for 2 h, 900 °C for 1 h and 1,100 °C for 10 min, and after wet chemical etching in hydrofluoric acid. The *vertical lines* represent the absorption bands corresponding to vibrations commonly observed in Si–C–H alloys: from *right* to *left*, Si–H wagging, Si–C stretching, C–H$_n$ wagging, Si–O stretching, Si–H$_n$ stretching, and C–H$_n$ stretching [21, 22]

3.2 Thermal Annealing

The formation of Si NCs starting from plasma-deposited SRC needs a high-temperature treatment in which the following phenomena take place: H evolution, phase separation of Si and SiC, SiC crystallization, and Si crystallization. These material transformations, except the Si crystallization, can be followed by Fourier transform infrared (FTIR) spectroscopy in the absorption modes. FTIR gives information on the atoms that compose the film as well as on the short- or medium-range order in a structure, being sensitive to the characteristic vibrations of atomic bonds. The absorption signal due to the homopolar Si–Si bonds is weak, because it results from a two-phonon process [20]. As a consequence, the contribution of the Si NCs to the absorption spectrum is negligible with respect to the one of the c-Si wafer substrates. Si–C bonds on the other hand exhibit a strong IR absorption which is readily monitored.

Figure 6.7 shows the mid infrared absorption spectra of 65-3-3 deposited on a 20 nm SiC crystallization barrier, as-deposited, after a series of thermal treatments (600, 900, and 1,100 °C) and after wet chemical etching. The spectra are corrected for substrate absorption, and a baseline is subtracted.

The spectrum of the as-deposited multilayer features broad absorption bands, indicating the structural disorder in the layer. The main peak at 773 cm^{-1} is due to the stretching of the Si–C bonds in disordered structures [21]. The other peaks give evidence of the high H content that is typical in PECVD prepared layers: the broad peak around 640 cm^{-1}, which appears as a shoulder of the main 770 cm^{-1} peak, is attributed to the wagging mode of the Si–H bond; the peak at 990 cm^{-1} is attributed

to vibrations of the C–H_2 wagging mode within $SiCH_2$ complexes; the signals at 2,080 cm^{-1} and around 2,800–3,000 cm^{-1} are corresponding to the Si–H_n and the C–H_n stretching bands, respectively [21, 22].

The spectrum of the film annealed at 600 °C presents sharper features. The Si–C peak is more pronounced as a consequence of the phase separation, and the H-related peaks have almost disappeared due to H effusion, with the exception of some residual signal at 640 and 2,070 cm^{-1} (Si–H bands) and 965 cm^{-1} (C–H_n band).

Complete H effusion is observed at 900 °C. Complete H effusion is detected at 900 °C. We also observe a wavelength shift of the Si–C stretching mode from 773 to 800 cm^{-1}, accompanied by a change in peak shape from Gaussian to Lorentzian. Both effects are due to crystallization of the SiC phase. When a material crystallizes, the bonds become stronger, leading to peak shift to higher wavenumbers, and the distribution of bond lengths and angles is no longer random but exhibits a preferred configuration due to the ordering in the crystalline lattice. The spectrum of the 1,100 °C annealed layer also presents this Lorentzian Si–C peak as well as an additional signal centered around 1,070 cm^{-1}, indicating the presence of a Si–O bonds. This signal is related to surface oxidation and is eliminated by etching the sample in diluted hydrofluoric acid [19], see Fig. 6.6.

3.3 Si Crystallization

The vibrational modes of the Si–Si bonds, that are almost inactive in the IR, are Raman active according to the "rule of mutual exclusion" which holds for centro-symmetric crystals like Si. Thus, Si crystallization can be investigated by Raman scattering. Amorphous and crystalline Si exhibit Raman peaks at 520 and 470 cm^{-1}, respectively, and deconvolving the two peaks allows for a quantification of the fraction of Si that has crystallized with respect to the total. Diffraction techniques, such as X-ray diffraction (XRD) and bright field transmission electron microscopy (TEM), can be used to get complementary information. XRD gives a spectrum with distinct peaks that can be attributed to Si and SiC using the Bragg equation. The height of the peaks represents the crystallized fraction, while the full width at half maximum can be used to determine the mean size of the Si and SiC nanocrystalline domains, using the Scherrer equation for the full width at half maximum of the (111) diffraction peak [23]. The diffraction pattern exhibited by the SiC component also allows for the identification of the SiC polytype resulting from SiC crystallization, which is the cubic polytype 3C-SiC [24, 25] for annealing temperatures up to 1,100 °C. TEM allows for direct imaging of the actual Si NC superlattice structure, i.e., the SiC barrier thickness, the distance between the nanodots, and the mean nanodot size. By TEM non-ideal features, such as nanocrystal outgrowth beyond the SRC layer, Si and C interdiffusion between adjacent layers and continuous Si crystallization in the SRC can also be detected.

Nanodot formation and crystallization in silicon carbide fabricated using the multilayer approach to control the nanodot size proceed in a different way than in the SiO_2 matrix. In the Si/SiO_2 case, the nanodot diameter is effectively controlled by the thickness of the silicon-rich oxide layer and is independent of the annealing duration [26]. Phase separation readily occurs [16], and no residual amorphous fraction is observed, provided that sufficiently high annealing temperature is used.

In contrast, in the Si/SiC case the nanodot size is not easily controlled. Random nanocrystal distribution and outgrowth of Si NCs over the SRC/SiC bilayer thickness are observed if improper conditions are used, as this leads to Si and C interdiffusion between adjacent layers [27]. Even a high residual amorphous silicon fraction is detected by Raman, depending on the design (x, d_{SRC}, and d_{SiC}) [13, 24, 28]. This observation was recently proposed [29] to show strong similarities with the case of Ge NC nucleation in SiO_2 [30].

For the Ge/SiO_2 case [30], it has been demonstrated that the high interface energy between c-Ge and SiO_2 leads to the development of an amorphous shell around the Ge NCs. The formation of the a-Ge shell creates an effective interface that lowers the overall energy [30, 31]. The same phenomenon is likely to occur in the Si/SiC system due to the remarkably high energy of the c-Si/SiC interface, which stems from the 19 % lattice mismatch.

For thick SRC layers continuous crystallization is favored with respect to NC formation due to the low distance between the crystal nuclei, which implies that too low an amount of Si atoms is remaining to form the shell needed for the stability of isolated nanocrystals [29, 30]. This observation is in contrast with the description for the formation of Si NCs in SiO_2 matrix (see Fig. 6.3), in which the thickness of the SRL determines the nanodot size. As a consequence, only a limited range of nanodot sizes is achievable in the Si/SiC system by the multilayer method.

Figure 6.8 shows energy-filtered (EF) TEM micrographs of two annealed multilayers, 75-3-3 (a) and 95-3-3 (b). The electron energy loss spectra are filtered around the 17 eV Si plasmon energy. The Si-rich regions appear brighter, while the SiC shows a darker contrast. The two materials differ by the SRC composition. After annealing only the multilayer with the higher x shows a multilayer structure. In [29] a lower limit of 2.5–3 nm and $x > 0.75$ are proposed for a control of the multilayer structure. This image highlights the importance of understanding the material evolution upon annealing for a proper multilayer design.

4 Optical Modeling

This section aims at describing a particular approach for thin-film structural characterization, based on the fitting of optical reflectance and transmittance (R&T) spectra. UV–vis spectroscopy generally supplies information on the optical absorption of a composite material as a whole. In this section it will be shown that fitting of the R&T spectra allows for the extraction of the relative volumes of the
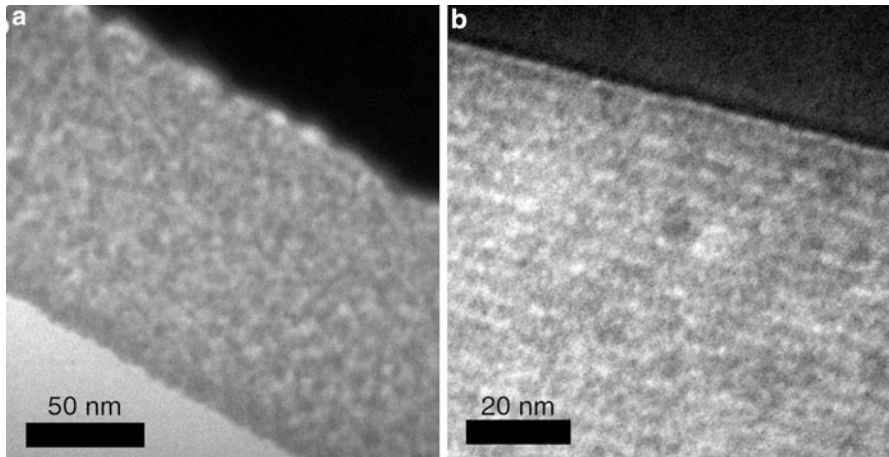
Fig. 6.8 EF-TEM micrographs of 75-3-3 (**a**) and 95-3-3 (**b**) after annealing at 1,100 °C. The Si-rich regions appear bright. The surface is on the *top right side* of the pictures

material subcomponents, SiC and Si, and for the amorphous and crystalline Si fractions of the total Si volume. This information can be used to extract the optical absorption of the sole Si component in the case of an absorbing matrix like SiC.

4.1 Introduction to the Method

The computer code Optical [32] calculates the R&T spectra of multilayer structures using a scattering matrix formalism for the light propagation. The interface matrix between two adjacent layers is defined using the Fresnel coefficient approach. The optical spectral functions for the wave propagation through a layer can take into account mixed-phase layers through the Bruggeman effective medium approximation (EMA). If the optical spectral functions of all the components are known, the software allows for the calculation of each layer composition and thickness using a χ^2 minimization.

However, proper spectral functions of the subcomponents of the multilayers at the different stages of the production process cannot be readily identified in the literature due to the high impact of the processing conditions on the optical properties of the material. This is especially true for SiC-based materials, i.e., the as-deposited a-Si_xC_{1-x}:H, the dehydrogenated amorphous SiC (a-SiC), and the crystallized SiC (μc-SiC) [14]. In order to extract unknown (n,k) functions, reference single layers of the involved materials were produced, and their R&T spectra were fitted using the computer program MinuitFit [33] that is based on a modified Tauc-Lorentz model [34]. It has to be noted, however, that this procedure assumes the equality of the optical properties of nanocrystals and of continuous nanocrystalline materials, which is not confirmed.
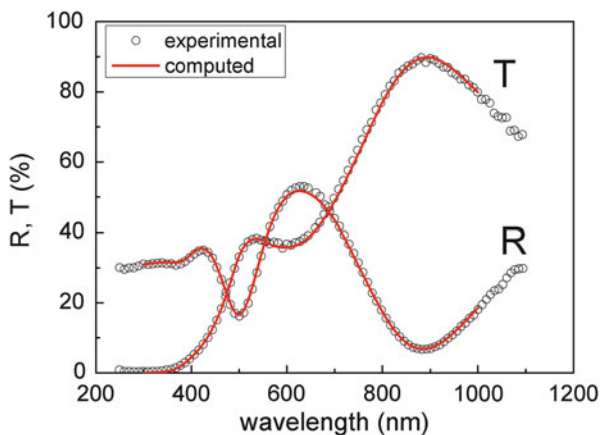
Fig. 6.9 Experimental and simulated R&T spectra of 65-3-5 after 1,100 °C annealing. The *symbols* are the measured spectra, and the *lines* are the computed spectra

The spectral data of the Si phases are drawn from [35] and [36]. The spectral data for SiO$_2$ are drawn from [37].

4.2 Modeling of SiC/Si NC Multilayers

The simulation of the annealed SiC/Si NC material is obtained by considering a stack of four layers: a low-density surface layer as residual from the wet etching sequence described in Sect. 3; the SiC/Si NC layer; the SiC crystallization barrier; and the substrate. The fitting procedure allows for the extraction of the thickness of each layer and the composition of the SiC/Si NC layer. The latter can be considered as an effective medium made up of μc-SiC, μc-Si, and a-Si. Based on the TEM diffraction patterns as well as the Lorentzian shape of the Si–C stretching band after thermal annealing at 1,100 °C the SiC sub-component is approximated as being completely microcrystalline. The assumption that the optical spectral functions of the Si NCs are the same as the ones of continuous nanocrystalline domains is made for simplicity but has an impact on the crystalline silicon fraction extracted by fitting of the R&T spectra.

Figure 6.9 shows as an example the R&T spectra measured on 65-3-5 deposited on a 20 nm SiC buffer layer and treated according to the sequence described in Fig. 6.6. The calculated spectra that best fit the experimental data are obtained for the following structure: 5 nm SiC surface, 133 nm SiC/Si NC, and 10 nm SiC crystallization barrier. The different structural features result in different signatures in the R&T spectrum: the fringe contrast in the region of transparency ($A = 0$ and $R + T \equiv 1$), that for the film in Fig. 6.9 lies between 700 and 1,000 nm, depends on the bulk refractive index and is therefore almost univocally related to the Si/SiC volume ratio. For a given Si/SiC ratio, the fringe period is univocally determined by

the thickness. The c-Si/a-Si ratio determines the onset and rise of transmittance, i.e., in particular the T maximum in the medium absorption wavelength range (500–700 nm in Fig. 6.9), in which the absorptivities of a-Si and μc-Si show considerable difference. The Si NC layer shown in Fig. 6.9 is composed by 70 % SiC, 22 % a-Si, and 8 % μc-Si.

The crystallized Si fraction, X_C, is given by the volume fraction of the crystallized Si divided by the total Si volume fraction:

$$X_c = \frac{V_{\mu c-\text{Si}}}{V_{\mu c-\text{Si}} + V_{a-\text{Si}}}. \qquad (6.3)$$

According to (6.3) 23 % of the Si component crystallized during annealing in the sample of Fig. 6.9. The X_C extracted from optical simulation can be compared to structural characterization obtained by Raman spectroscopy. [28, 29] provide a comparison between the crystallized Si fraction obtained by the fitting of R&T spectra and by Raman spectroscopy. The results obtained by the two techniques are in good qualitative agreement. The absolute values of the Si crystallized fraction depend on the choice for the Si NC optical functions.

In conclusion, UV–vis R&T spectra provide a wide range of structural information about Si NC films when complemented with an optical simulation and can be used to determine the absorption properties in view of PV application.

4.3   Optical Properties of Nanocrystals

Following the scenario illustrated in Sect. 1, the ideal optical properties of Si NCs used as absorber material in the top device of a tandem solar cell should show a complete transparency for $E < E_g$ and a high absorption for $E > E_g$. The actual absorption spectrum of nanocrystals is still a matter of debate for a number of reasons. First, as it is correlated to the quantum confinement-related energy-level splitting, it depends on diameter, with related consequences for non-spherical nanocrystals. Secondly, as it is affected by the bonding configuration of atoms at the nanocrystal surface, it is sensitive to the environment [38]. Third, the application in solar cell devices implies attention to the absorption region just above gap, since ideal energy conversion can be obtained only in this energy range, see Fig. 6.1. The absorption of photons whose energy lies in this region is limited by the density of states and can be characterized with only moderate accuracy by a standard optical technique like ellipsometry. Several references exists on the topic, see for example [39–42], mostly focusing on the high-absorption region. In the medium-absorption region the most informative is probably [39]. An optical model for the medium-absorption region was recently proposed by Allegrezza et al. [43]. In the framework of the SiC/Si NC system, the precise determination of the absorption spectrum is complicated by the non-negligible band tail and the defect absorption in SiC [14].
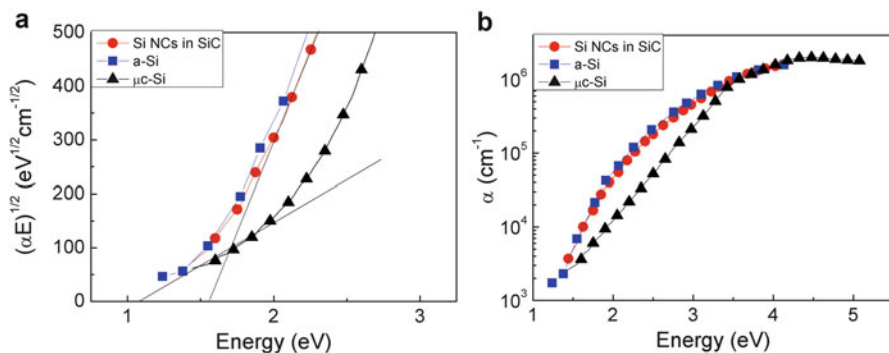
Fig. 6.10 (**a**) Tauc plot and (**b**) absorption spectra of the Si nanodot component in the SiC/Si NCs film of Fig. 6.9 and of a-Si [36] and μc-Si [35]

Figure 6.10a reports the Tauc plot for the sole Si component obtained from the simulation of the R&T spectrum in Fig. 6.9. The Tauc plot of a-Si [36] and μc-Si [35] are also reported for comparison. The Si nanodot component in the multilayer shows $E_g = 1.5$ eV that represents a blue shift with respect to the microcrystalline value. However, the absorption spectrum appears to be dominated by the amorphous component also detected by Raman. Figure 6.10b shows the absorption coefficient for the same materials. For energies above the bandgap, the Si nanodots exhibit an increased absorption with respect to microcrystalline silicon. This has a positive impact for solar cell devices, as it allows for the lowering of the absorber layer thickness provided that carrier lifetime is not severely limited by recombination in the amorphous phase.

5 Device Characterization

The concept of characterizing the Si NC film without any wafer influence using the membrane device structure introduced in Sect. 2 depends critically on the electrical insulation properties of the insulation layers. To ensure reliable characterization of the Si NC p-i-n diode it must first be proven electrically that for each structure the photovoltage and the photocurrent stem only from the "membrane diode" itself and not from the wafer. Only then further characterization can be carried out.

A potential contribution of the wafer to the photovoltaic properties of the overall device can be thought of as an additional "wafer diode" in parallel to the "membrane diode." In order to separate the membrane diode characteristics from the "wafer diode," the different device parts were illuminated separately and the overall *IV* curve was measured. In principle the device can be illuminated from either side. In order to demonstrate the device functionality, however, the structured and therefore critical side was illuminated to more readily detect a possible contribution of the wafer.
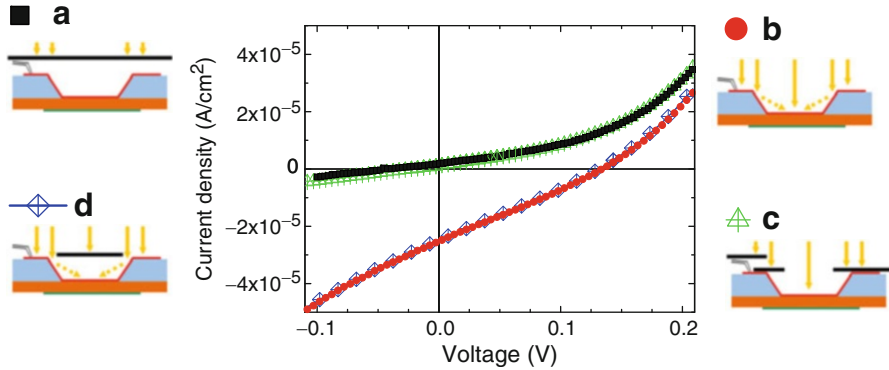
Fig. 6.11 Current–voltage curves of a malfunctioning membrane cell in dark (**a**), under full area illumination (**b**), and under illumination with shadow masks (**c**, **d**). The figure was taken from [2]
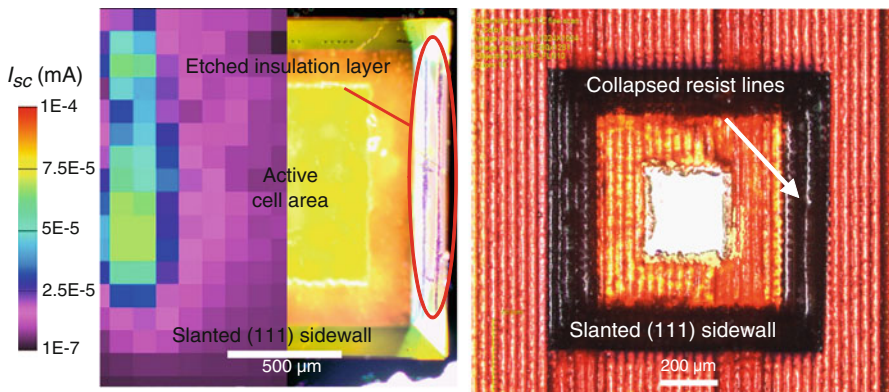

Fig. 6.12 (*Left*) Light beam-induced current (LBIC) map combined with the dark field micrograph of a malfunctioning membrane-based p-i-n solar cell. The LBIC map is mirrored along the *vertical center line*. The area of maximum current corresponds to the etched insulation layer. (*Right*) Optical micrograph of an inkjet printed membrane before structuring of insulation layer B (process step 13, cf. Fig. 6.5). The figure was taken from [2]

Figure 6.11 shows *IV* curves of one membrane cell in the dark (A), under illumination of the entire wafer (B), and under illumination with shadow masks (C, D). Mask C leaves only the membrane illuminated but shadows the surrounding wafer and contacts. Under mask D, only the "wafer diode" is illuminated and light can reach the membrane cell only by reflection at the slanted sidewalls. For the cell shown here, the *IV* curve with mask D reproduces the *IV* curve under full area illumination. This hints at a damaged insulation layer and a large wafer contribution to the overall *IV* curve.

A powerful tool to investigate the spatially resolved charge carrier collection properties and local shunting is light beam-induced current (LBIC) mapping. Figure 6.12 (left) shows an LBIC map along with the (mirrored) dark field optical
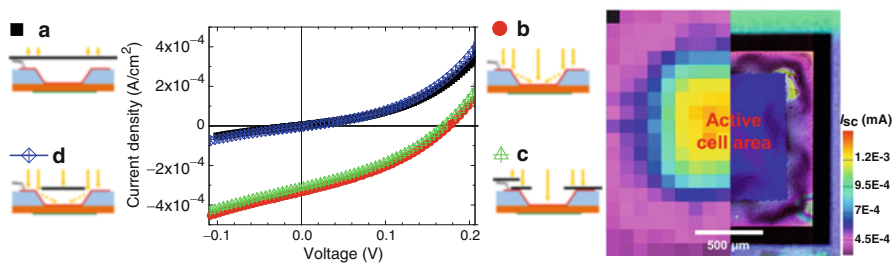
Fig. 6.13 (*Left*) Current–voltage curves of a correctly functioning membrane cell in dark (**a**), under full area illumination (**b**), and under illumination with shadow masks (**c**, **d**). (*Right*) Light beam-induced current map of the corresponding cell combined with an optical micrograph (*mirrored*). The figure was taken from [2]

micrograph of the same cell whose *IV* curves were shown in Fig. 6.11. A photocurrent from the slanted sidewalls can be seen in the LBIC image. In exactly this area the dark field image reveals two line-shaped etch-damaged regions. The insulation layer B is damaged here, giving rise to photocurrent collection from the wafer substrate in this area. Figure 6.12 (right) depicts an optical micrograph of an identically processed structure in step 13 of the fabrication process. The inkjet resist is printed in lines from a print head that moves in one direction over the sample. The typical line pattern of the inkjet resist can be seen in Fig. 6.12 (right) on the wafer surface, the membrane, and the slanted sidewalls. However, the line pattern exhibits a different period on the slanted sidewall on the right-hand side. Several ink lines merged here because the inkjet resist droplets rolled down the steep (54.7°) sidewalls. Hence, it can be concluded from the line pattern in Fig. 6.12 (left) that the insulation layer damage seen was caused by a collapse of the inkjet resist lines on the slanted sidewalls as seen in Fig. 6.12 (right). The line-shaped etch damage can thus be attributed to failure of the inkjet resist during wet chemical etching in step 13 or 15 (flow chart in Fig. 7.4).

The systematic study of all structures with light microscopy and LBIC supplemented by electron beam-induced current studies for selected structures as reported in [7] allows a clear identification of correctly functioning devices. After selection of those devices that appeared to be free of defects in the light microscope, a clear correlation was established between the results of *IV* and LBIC measurements. When an *IV* curve was attributed to the membrane but not the wafer based on the shadow mask procedure, LBIC measurements confirmed this behavior. An example of this behavior is shown in Fig. 6.13. The *IV* curve with shadow mask D resembles the dark *IV* curve very well, and the application of mask C demonstrates that the *IV* curve is due to the active cell area on the membrane only. The LBIC map (Fig. 6.13 right) finally confirms this behavior.

Based on these experiments, the following procedure was established: in a first step, all devices are analyzed by optical microscopy with special emphasis on the upper sidewall rims. Then, the insulation layer on the slanted sidewalls is checked

with dark field microscopy. If the structure appears to be free of defects, *IV* curves in dark, under full area illumination, and with shadow masks C and D are measured. If the *IV* curves demonstrate that the wafer does not influence the measurement, the structure is qualified as "good" and selected for further characterization.

EBIC and LBIC are current-sensitive methods and do not provide information on the magnitude of the photovoltage. The latter is provided by *IV* measurements employing shadow masks as shown in Figs. 6.11 and 6.13. However, the shadow mask method does not allow the identification of a potential contribution from the slanted sidewalls. Therefore, the *IV* characteristics of the entire structure were simulated for different cases of failing insulation layers. The simulation demonstrates that the photocurrent of the *IV* curve is indeed sensitive to an insulation layer failure. As the photovoltage was shown to be much less sensitive to insulation layer failure, current-sensitive methods such as LBIC or EBIC are viable tools to prove the origin of both the photocurrent and the photovoltage. Differently put, the simulations showed that if the photocurrent can be shown to originate from the membrane only, then the same can be assumed for the photovoltage.

6   Solar Cell Modeling

The optical absorption properties of the SiC/Si NC material extracted by UV–vis spectroscopy can be used to analyze the results obtained on membrane solar cell devices. Possible variations to the actual device structure are examined, with the aim of maximizing the fraction of light absorbed by the NCs.

6.1   Light Absorption in Individual Layers

As shown in Fig 6.4, the solar cell is schematically represented as a multilayer where the SiC/Si NC layer is embedded between two 10 nm thick SiC layers that account for the SiC crystallization barrier and the surface layer. The structure is completed on both sides by an a-$Si_{0.95}C_{0.05}$ doped layer (20 and 25 nm on the top and on the back side, respectively) and an ITO layer (70 nm).

The upper limit for the short-circuit current, J_{gen}, of the device is determined by the overlap integral of the calculated absorptance of the membrane with the AM1.5G solar spectrum, under the assumption of a complete collection of electron/hole pairs generated in the SiC/Si NC absorber. The light absorbed in the doped layers should not contribute to the photocurrent due to the short minority carrier lifetime in highly doped materials.

The absorption spectrum of individual layers and the resulting global absorption of the membrane are shown in Fig. 6.14a.
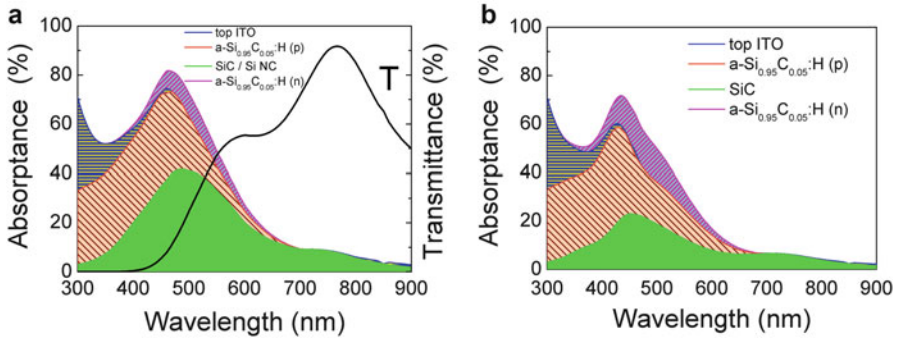
Fig. 6.14 (**a**) Computed transmittance spectrum (*black line*) of the membrane solar cell characterized in Sect. 5 and computed absorption spectrum of the entire device as the sum of the absorption in individual layers. (**b**) Computed absorption spectrum of a device with a SiC absorber (without Si NCs)

The calculated J_{gen} for this structure is 5.97 mA/cm^2, represented by the green area in Fig 6.14a. The discrepancy between the theoretical and the experimental value is discussed in Sect. 7.

For comparison, the same calculation, yet having removed the Si NCs from the SiC layer, is reported in Fig. 6.14b. In this case, J_{gen} is 3.1 mA/cm^2. It can be seen that the spectral shapes of the two cases (with and without NCs, panels a and b, respectively) are similar. However, the presence of Si NCs clearly enhances the absorption of light in the absorber layer and the overall structure.

6.2 Optimization of the Optical Properties

The identification of the contributions of each single layer to the overall absorption is the basis for the optimization of the device structure for future developments. It is apparent from Fig. 6.14a that a significant fraction of the incident light is lost in the top doped layer. Moreover, a significant fraction of light is transmitted through the device without generating any current. Popular solutions in the world of thin-film solar cells are the use of a window layer as front doped layer as well as a back stack based on a metal reflector [44].

A window layer is a high-bandgap doped material, typically p-doped a-Si$_x$C$_{1-x}$. The high-bandgap guarantees better transparency, yet with the drawback of less effective doping for increasing carbon content. A trade-off is therefore needed for the composition. Reducing the thickness also contributes to enhancing transparency. However, the window layer should not be thinner than the depletion region to avoid deterioration of the open-circuit voltage [45]. Within this context and taking advantage of preliminary optical characterization of a-Si$_x$C$_{1-x}$ materials, we used optical simulation to compute the impact of composition and thickness of the window layer on J_{gen}. The results are reported in Fig. 6.15a.
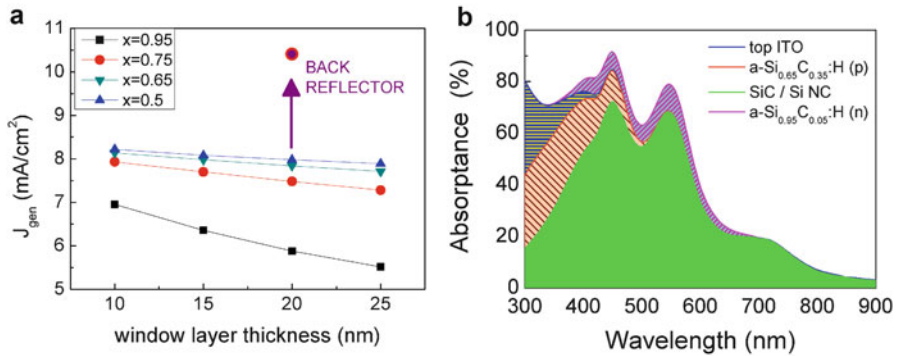
Fig. 6.15 (**a**) Computed J_{gen} for different top layer compositions and thicknesses. The further enhancement of J_{gen} when adding a back reflector is shown by a *circle*. (**b**) Computed absorption in the SiC/Si NC layer within the optimized solar cell structure including the back reflector (indicated by an *arrow* in (**a**))

The figure shows that a slightly higher carbon content in the top a-Si_xC_{1-x}:H (p) layer (the hole collector) is already effective in increasing J_{gen}. The effect saturates with higher x. Moreover, J_{gen} shows little dependence on thickness, indicating that the larger thicknesses needed to guarantee higher built-in voltages will be only negligibly detrimental to the device. A reduction of transmission losses is predicted by introduction of a 30 nm silver back reflector that results in an increase of absorption in the SiC/Si NC layer by 30 %.

Figure 6.15b shows the computed absorption in the NC layer for the optimized structure including the back reflector. The fraction of light absorbed by the NC layer with respect to the total is higher due to the combined action of the wider bandgap of the window layer and of the back side mirror, indicating a possible improvement in the design of the device. The computed J_{gen} for this structure is 10.4 mA/cm^2.

7   Recombination and Transport Properties of Silicon Nanocrystals in SiC

Typical *IV* curves in dark and under illumination (light *IV* curve) of a membrane p-i-n solar cell are shown in Fig. 6.16. The membrane p-i-n solar cell was designed as depicted in Figs. 6.4 and 6.5 with the resulting optical properties presented in Fig. 6.14a. The measurements were taken at a sample temperature of 25 °C, and the illumination was set to 1,000 W/m^2 unless otherwise specified. The open-circuit voltage V_{OC} of the cell shown in Fig. 6.16 is 282 mV, and the short-circuit current density J_{SC} is 0.339 mA/cm^2. The fill factor (FF) is 36.2 %. The light *IV* curve in Fig. 6.16 exhibits a pronounced slope at 0 V, i.e., a short-circuit conductance, which is not present in the dark curve. The dark and light curves are also seen to cross over
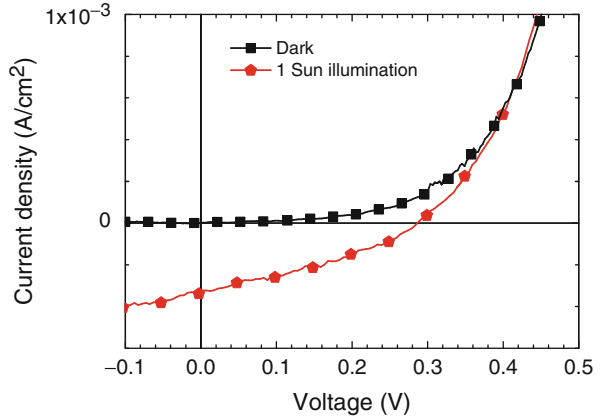
at a voltage of 400 mV. The crossover is a common feature for Si and chalcopyrite thin-film solar cells [46] and can be explained with a photo shunt or a voltage-dependent current collection function. The experimental J_{SC} value is only $0.06 \times J_{gen}$, indicating highly recombinative defects in the Si NC layer. The characteristics of the *IV* curves shown in Fig. 6.16 (shunt under illumination, crossover of light and dark *IV* curves, fill factor, J_{SC} and V_{OC} values) are typical for all membrane cell devices investigated.

The peculiar *IV* characteristics (shunting, high series resistance, low fill factor) do not permit an unequivocal fit of the one-diode model to the data as it is usually done for c-Si solar cells. Therefore, a detailed *IV* curve analysis must be undertaken. First, the dark curve is analyzed to determine the series resistance, parallel resistance, and ideality factor. In a second step, the dark diode parameters are used to fit the light *IV* curve according to the uniform field approximation assuming validity of the superposition principle [ref to theory].

The dark parallel resistance $R_P = 11{,}808\ \Omega\ \text{cm}^2$ is calculated from the slope of the dark *IV* curve around 0 V (short-circuit resistance). The series resistance and diode ideality factor are then extracted using the small conductance method after Werner [47].

Having these parameters fixed, illumination-dependent *IV* measurements are employed with the objective to determine the effective mobility lifetime product $(\mu\tau)_{eff}$, which is a fundamental transport and recombination property of the material.

IV curves at illumination levels between 1 and 20 suns are shown in Fig. 6.17. The illumination level was adjusted with a Fresnel lens with variable distance to the sample.

All light *IV* curves in Fig. 6.17 exhibit a pronounced photo shunt indicating strong recombination in the Si NC layer. The following analysis is governed by the idea of a thin, undoped, and recombinative absorber within the electrical field between the highly doped regions. This case can be described with reasonable
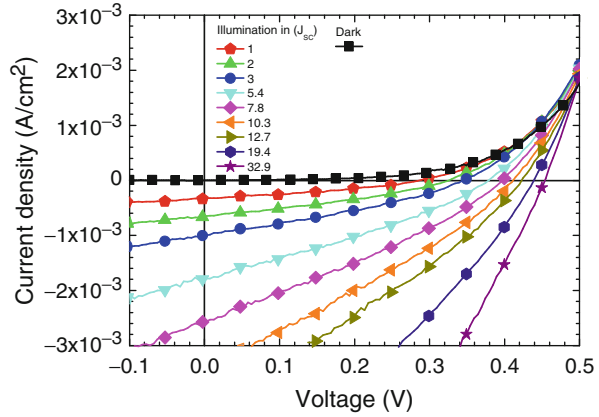
simplifications using the uniform field approximation introduced by Crandall [48], which leads to a voltage-dependent photocurrent collection function $\chi(V)$, given by

$$\chi(V) = \frac{L_D}{d}\left(1 - \exp\left(-\frac{d}{L_D}\right)\right), \qquad (6.4)$$

where d is the absorber thickness. The voltage dependency of the photocurrent collection function is "hidden" in the effective drift length L_D,

$$L_D = (\mu\tau)_{\text{eff}}(V_{FB} - V)/d, \qquad (6.5)$$

which describes the mean distance that a charge carrier will travel by drift in the electric field in the solar cell absorber before recombination. At flat band conditions (when the external voltage V equals the flat band voltage V_{FB}) the electric field is zero, drift does not occur, charge carriers do not reach the contacts anymore, and the photocurrent is zero. Hence, the dark current equals the light current J_{light} at that voltage, or differently put, V_{FB} is the voltage where the light and dark IV curves cross over.

The IV curve is defined by the collection function $\chi(V)$ as well as the parameters of the common one-diode model, which are the saturation current density J_0, the ideality factor n, the series resistance R_S, the parallel resistance R_P, and the Boltzmann constant k_B:

$$J_{\text{light}}(V) = J_0\left(\exp\left(\frac{qV}{k_B T}\right) - 1\right) + \frac{V}{R_P} - J_{\text{gen}}\chi(V). \qquad (6.6)$$

The advantage of the uniform field approximation is that it permits the analytical description of the entire light IV curve between short-circuit and open-circuit or crossover conditions. The light IV curve after (6.6) involves eight parameters (J_{gen}, J_0, n, R_S, R_P, V_{FB}, $(\mu\tau)_{\text{eff}}$, d). As mentioned before, R_S, R_P, and n were determined
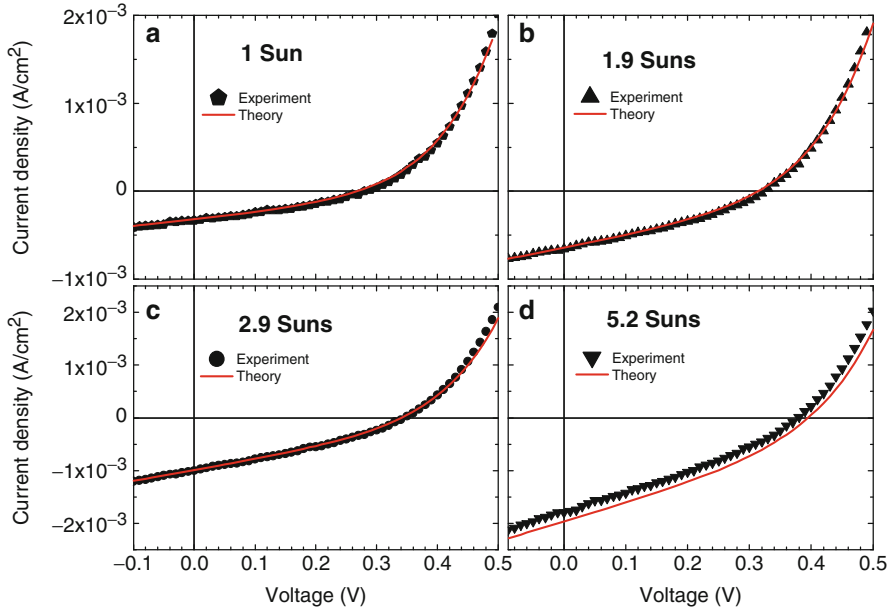
Fig. 6.18 Current–voltage curves of membrane-based p-i-n devices and the respective fits of the one-diode model with a voltage-dependent current collection function in the uniform field approximation [(6.6) with the collection function of (6.4)] to the data. Series resistance, parallel resistance, and ideality factor were fixed to the dark values. Reprinted with permission from [9]. Copyright 2013, American Institute of Physics

from the dark IV curve with the analysis after Werner [47], and V_{FB} was obtained from the crossover voltage. The absorber layer thickness and the maximum short-circuit current were obtained from the optical simulation discussed above. This procedure means that only J_0 and $(\mu\tau)_{eff}$ need to be fitted to the light IV curve (6.6). For an unequivocal determination of these two parameters, illumination-dependent current–voltage measurements were carried out and fitted simultaneously with the same set of parameters according to (6.6) (Fig. 6.18).

The illumination was set to $C \times J_{gen}$, where C is the light concentration calculated from the ratio of the respective short-circuit current and that under 1 sun illumination. The optical limit (5.97 mA/cm^2, see Sect. 6) was used for J_{gen} at 1 sun illumination. The flat-band voltage was set to $1.2 \times V_{CO}$ for the best fit, where V_{CO} refers to the crossover voltage determined from Fig. 6.17. An excellent fit is obtained for a wide range of illumination intensities with $(\mu\tau)_{eff} = 2.6 \times 10^{-11}$ cm^2/V and $J_0 = 5.2 \times 10^{-6}$ A/cm^2. The only parameter that is not confirmed independently is the dark saturation current. However, Hegedus [46] analyzed data from a large variety of thin-film solar cells and demonstrated that within a regime in which V_{OC} is linearly correlated with V_{FB}, the dark saturation current does not influence V_{OC}. As the IV curves presented here exhibit a linear dependence of V_{OC} on V_{FB} (not shown explicitly), it was concluded that J_0 only has a minor impact on V_{OC}.
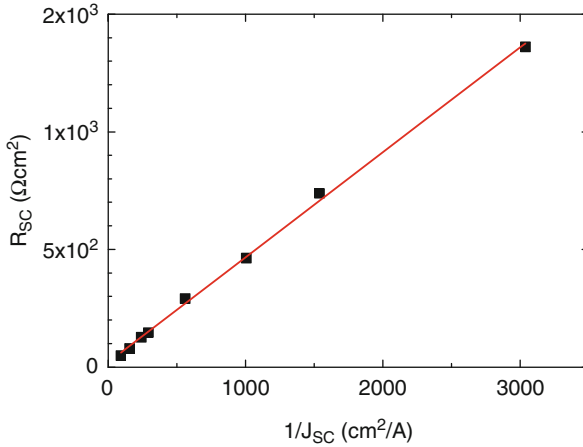
Fig. 6.19 Illumination dependence of the short-circuit resistance (*points*), and fit of (6.7) to the data. The slope of the linear regression is 0.3932 V. This corresponds to $(\mu\tau)_{\text{eff}} = 5.75 \times 10^{-10}$ cm^2/V and an effective drift length of 150 nm with $V_{\text{FB}} = 0.4$ V at zero applied bias. Reprinted with permission from [9]. Copyright 2013, American Institute of Physics

The good agreement between the experimental data and the theory over a wide range of illumination densities (Fig. 6.18) strongly supports the validity of the presented analysis.

Complementary to the application of the uniform field approximation after Crandall, the analysis after Merten et al. [49] was applied. The latter is restricted to zero bias and results in the following expression for the short-circuit resistance R_{SC}:

$$R_{\text{SC}} = \left(\frac{\text{d}J}{\text{d}V}\right)^{-1}\Bigg|_{V=0V} = \frac{1}{J_{\text{SC}}}\frac{(\mu\tau)_{\text{eff}}V_{\text{FB}}^2}{d^2} = \frac{L_{\text{D}}(V=0V)V_{\text{FB}}}{J_{\text{SC}}d}. \tag{6.7}$$

The effective drift length L_{D} is defined as in (6.5). As this analysis utilizes only directly accessible *IV* curve parameters, no *IV* curve fit is necessary. Equation (6.7) illustrates that the recombination appears in the *IV* curve as an illumination-dependent short-circuit resistance. The method can be used to extract the drift length from the slope of a plot of R_{SC} over $1/J_{\text{SC}}$. The illumination dependence of R_{SC} is depicted in Fig. 6.19. The experimental data obey (6.7) very well, and a linear regression yields a slope of 0.3932 V. This corresponds to an effective drift length of 150 nm and an effective mobility lifetime product of $(\mu\tau)_{\text{eff}} = 5.75 \times 10^{-10}$ cm^2/V at short-circuit conditions and with V_{FB} set to equal the crossover voltage (0.4 V).

Furthermore, the mobility lifetime product agrees within one order of magnitude with the value of $(\mu\tau)_{\text{eff}} = 2.6 \times 10^{-11}$ cm^2/V derived with the method after Crandall (cf. Fig. 6.18). The method after Merten et al. does not require knowledge of J_{gen} but utilizes only the directly accessible J_{SC}. On the other hand, the optical limit was assumed for J_{gen} for the *IV* curve fitting. As the optical limit is the ideal

Illumination-dependent IV analysis

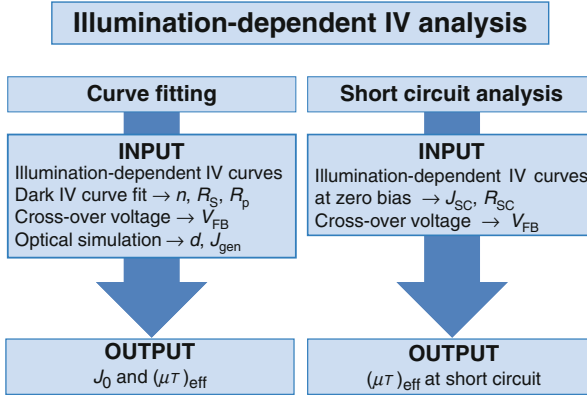| Curve fitting	Short circuit analysis
INPUT	**INPUT**
Illumination-dependent IV curves	Illumination-dependent IV curves
Dark IV curve fit $\rightarrow$ n, R_S, R_p	at zero bias $\rightarrow$ J_{SC}, R_{SC}
Cross-over voltage $\rightarrow$ V_{FB}	Cross-over voltage $\rightarrow$ V_{FB}
Optical simulation $\rightarrow$ d, J_{gen}	
OUTPUT	**OUTPUT**
J_0 and $(\mu\tau)_{eff}$	$(\mu\tau)_{eff}$ at short circuit

Fig. 6.20 Procedures for the illumination-dependent *IV* curve analysis. Simultaneous *IV* curve fits at various illumination levels yield the effective mobility lifetime product and the saturation current density. An analysis of the dark *IV* curve and an optical simulation are the prerequisites of this approach. A simplified procedure, whose validity is restricted to zero bias, is possible by analyzing the illumination dependence of the short-circuit parameters R_{SC} and J_{SC}

case it overestimates J_{gen}, and the procedure thus underestimates $(\mu\tau)_{eff}$ for a given short-circuit current. Thus, the analysis after Crandall is expected to yield a lower $(\mu\tau)_{eff}$ value than the method after Merten. Given the very limited foreknowledge about the Si NC material, both theories are in excellent agreement.

Figure 6.20 compares the required input parameters and the validity of the two procedures. The detailed curve fitting (Fig. 6.18) requires an analysis of the dark *IV* curve as well as an optical simulation of the entire device. The short circuit analysis on the other hand constitutes a simplified approach whose validity is restricted to zero bias. It makes use of the illumination dependence of R_{SC} and J_{SC}, which are both readily accessible *IV* curve parameters.

Both methods employed here ascribe any recombination in the entire device to the effective mobility lifetime product. As losses can also occur in the other device parts apart the Si NC absorber, e.g., by interface recombination or transport barriers, the value of $(\mu\tau)_{eff} \approx 10^{-10}$ cm^2/V has to be seen as a lower limit to the electronic quality of the Si NC film itself.

8   Conclusion

The implementation of Si NCs as the top solar cell absorber is a promising solution to realize a crystalline silicon tandem solar cell. Especially attractive is the fabrication of Si NCs in a Si-based matrix as this approach is compatible with Si technology and photovoltaic production equipment.

In this chapter, the fabrication of Si NCs in a SiC matrix and its characterization as a solar cell absorber have been discussed. Different formation mechanisms

have been identified with respect to the case of a SiO_2 matrix. The ordered growth that takes place in SiO_2/SRO multilayers appears to be perturbed by the high c-Si/SiC interface energy, so size control in SiC/SRC multilayers is achieved only for particular conditions. From the optical point of view, Si NCs have demonstrated better absorption properties with respect to bulk silicon. However, the high volume fraction of residual amorphous phases detected by optical spectroscopy stresses the importance of further optimizing the crystallization process in order to avoid possible degradation of the electronic properties by the defect-rich dehydrogenated a-Si.

Furthermore, a membrane-based test device has been presented that enables the characterization of Si NC films on device level free of any substrate influence.

The membrane-based test device decouples the high-temperature annealing step from the formation of electron and hole collectors (doped regions) and thus enables for the first time a substrate-free photovoltaic characterization of Si NC films.

A detailed photovoltaic characterization was carried out with the aim to characterize the mobility lifetime product on device level. For this means, illumination-dependent IV measurements were analyzed in the framework of the uniform field approximation. An optical characterization and simulation were employed to extract the absorption of the Si NCs and of the SiC matrix and thus to derive an upper limit for the photogenerated current in the membrane p-i-n solar cell. The upper limit of the photogenerated current was used for the analysis of the illumination-dependent IV curves, and excellent agreement between experimental data and theory was found over a wide range of illumination intensities. The photovoltaic performance was found to be limited by charge carrier recombination. A lower limit of the effective mobility lifetime product in the order of 10^{-10} cm^2/V was derived.

The procedure presented here, the illumination-dependent analysis of membrane-based Si NC p-i-n solar cells in conjunction with an elaborated optical device model, presents a powerful characterization scheme for Si NC solar cells. Si NC materials have so far been developed based on an optimization of their structural properties. The next step is to apply the characterization scheme discussed in this chapter to various Si NC materials for a comprehensive material development on the electrooptical level with the target of implementing Si NCs to the crystalline Si tandem solar cell.

References

1. Glunz, S.W., Preu, R., Biro, D.: Crystalline silicon solar cells: state-of-the-art and future developments. In: Sayigh, A. (ed.) Comprehensive Renewable Energy, vol. 1, pp. 353–387. Elsevier, Oxford (2012)

2. Löper, P.: Silicon nanostructures for photovoltaics. Dissertation in submission, Universität Freiburg, Freiburg, Germany (2013)
3. Green, M.A., Emery, K., Hishikawa, Y., Warta, W., Dunlop, E.D.: Solar cell efficiency tables (version 41). Prog. Photovolt. Res. Appl. **21**(1), 1–11 (2013)
4. Staebler, D.L., Wronski, C.R.: Reversible conductivity changes in discharge-produced amorphous Si. Appl. Phys. Lett. **31**(4), 292–294 (1977)
5. Lee, B.G., Hiller, D., Luo, J.-W., Semonin, O.E., Beard, M.C., Zacharias, M., Stradins, P.: Strained interface defects in silicon nanocrystals. Adv. Funct. Mater. **22**(15), 3223–3232 (2012)
6. Cuevas, A.: Misconceptions and misnomers in solar cells. In: Proceedings of the 26th European Photovoltaic Solar Energy Conference, Frankfurt, Germany, 2012
7. Löper, P., Canino, M., Lopez-Vidrier, J., Schnabel, M., Schindler, F., Heinz, F., Witzky, A., Bellettato, M., Allegrezza, M., Hiller, D., Hartel, A., Gutsch, S., Hernandez, S., Guerra, R., Ossicini, S., Garrido, B., Janz, S., Zacharias, M.: Silicon nanocrystals from high-temperature annealing: characterization on device level. Phys. Status. Solidi. **A210**, 669–675 (2013)
8. Löper, P., Stüwe, D., Künle, M., Bivour, M., Reichel, C., Neubauer, R., Schnabel, M., Hermle, M., Eibl, O., Janz, S., Zacharias, M., Glunz, S.W.: A membrane device for substrate-free photovoltaic characterization of quantum dot based p-i-n solar cells. Adv. Mater. **24**, 3124–3129 (2012)
9. Löper, P., Canino, M., Qazzazie, D., Schnabel, M., Allegrezza, M., Summonte, C., Glunz, S.W., Janz, S., Zacharias, M.: Silicon nanocrystals embedded in silicon carbide: investigation of charge carrier transport and recombination. Appl. Phys. Lett. **102**(033507), 1–4 (2013)
10. Zacharias, M., Heitmann, J., Scholz, R., Kahler, U., Schmidt, M., Bläsing, J.: Size-controlled highly luminescent silicon nanocrystals: a SiO/SiO_2 superlattice approach. Appl. Phys. Lett. **80**(4), 661–663 (2002)
11. Song, D., Cho, E.-C., Conibeer, G., Cho, Y.-H., Huang, Y.: Fabrication and characterization of Si nanocrystals in SiC matrix produced by magnetron cosputtering. J. Vac. Sci. Tech. B **25**(4), 1327–1335 (2007)
12. Cheng, Q., Tam, E., Xu, S., Ostrikov, K.K.: Si quantum dots embedded in an amorphous SiC matrix: nanophase control by non-equilibrium plasma hydrogenation. Nanoscale **2**(4), 594–600 (2010)
13. Künle, M., Kaltenbach, T., Löper, P., Hartel, A., Janz, S., Eibl, O., Nickel, K.-G.: Si-rich a-SiC:H thin films: structural and optical transformations during thermal annealing. Thin Solid Films **519**(1), 151–157 (2010)
14. Summonte, C., Canino, M., Allegrezza, M., Bellettato, M., Desalvo, A., Mirabella, S., Terrasi, A. Systematic characterization of silicon nanodot absorption for third generation photovoltaics. In: Proceedings of the 26th European Photovoltaic Solar Energy Conference, Hamburg, Germany, 21–25 Sept 2011, pp. 361–6
15. Kurokawa, Y., Miyajima, S., Yamada, A., Konagai, M.: Preparation of nanocrystalline silicon in amorphous silicon carbide matrix. Jpn. J. Appl. Phys. **45**(40), 1064–1066 (2006)
16. Summonte, C., Desalvo, A., Canino, M., Allegrezza, M., Rosa, M., Ferri, M., Centurioni, E., Terrasi, A., Mirabella, S. Optical properties of silicon nanodots in SiC matrix, In: 25th European Photovoltaic Solar Energy Conference and Exhibition, Valencia, Spain, 2010
17. Shukla, R., Summonte, C., Canino, M., Allegrezza, M., Bellettato, M., Desalvo, A., Nobili, D., Mirabella, S., Sharma, N., Jangir, M., Jain, I.P.: Optical and electrical properties of Si nanocrystals embedded in SiC matrix. Adv. Mater. Lett. **3**(4), 297–304 (2012)
18. Schnabel, M., Löper, P., Gutsch, S., Wilshaw, P.R., Janz, S.: Thermal oxidation and encapsulation of silicon–carbon nanolayers. Thin Solid Films **527**, 193–199 (2013)
19. Canino, M., Summonte, C., Allegrezza, M., Shukla, R., Jain, I.P., Bellettato, M., Desalvo, A., Mancarella, F., Sanmartin, M., Terrasi, A., Löper, P., Schnabel, M., Janz, S.: Identification and tackling of a parasitic surface compound in SiC and Si-rich carbide films. Mater. Sci. Eng. B **178**, 623–629 (2013)
20. Johnson, F.A.: Lattice absorption bands in silicon. Proc. Phys. Soc. **73**, 265 (1959)

21. Kaneko, T., Nemoto, D., Horiguchi, A., Miyakawa, N.: FTIR analysis of a-SiC:H films grown by plasma enhanced CVD. J. Cryst. Growth **275**(1–2), e1097–e1101 (2005)
22. Summonte, C., Rizzoli, R., Bianconi, M., Desalvo, A., Iencinella, D., Giorgis, F.: Wide bandgab silicon-carbon alloys deposited by very high frequency plasma enhanced chemical vapor depisition. J. Appl. Phys. **96**(7), 3987–3997 (2004)
23. Scherrer, P.: Göttinger Nachrichten Gesellschaft **2**, 98 (1918)
24. Song, D., Cho, E.-C., Cho, Y.-H., Conibeer, G., Huang, Y., Huang, S., Green, M.A.: Evolution of Si (and SiC) nanocrystal precipitation in SiC matrix. Thin Solid Films **516**, 3824–3830 (2008)
25. Summonte, C., Canino, M., Allegrezza, M., Bellettato, M., Desalvo, A., Shukla, R., Jain, I.P., Crupi, I., Milita, S., Ortolani, L., López-Conesa, L., Estradé, S., Peiró, F., Garrido, B.: Boron doping of silicon rich carbides: electrical properties. Mater. Sci. Eng. B **178**, 551–558 (2013)
26. Hiller, D., Goetze, S., Zacharias, M.: Rapid thermal annealing of size-controlled Si nanocrystals: dependence of interface defect density on thermal budget. J. Appl. Phys. **109** (5), 054308–054308-5 (2011)
27. Künle, M.T.: Silicon carbide single and multilayer thin films for photovoltaic applications. Dissertation, Universität Tübingen, Tübingen, Germany (2011)
28. López-Vidrier, J., Hernández, S., Samà, J., Canino, M., Allegrezza, M., Bellettato, M., Shukla, R., Schnabel, M., Löper, P., López-Conesa, L., Estradé, S., Peiróa, F., Janz, S., Garrido, B.: Structural, optical and electrical properties of silicon nanocrystals embedded in SixC1 − x/ SiC multilayer systems for photovoltaic applications. Mater. Sci. Eng. B **178**, 639–644 (2013)
29. Hernandez, S., Summonte, C., Allegrezza, M., Bellettato, M., Liscio, F., Canino, M., Desalvo, A. Space of formation of silicon nanocrystals in silicon carbide, In: Proceedings of the E-MRS Spring Meeting, Strasbourg, France (2013)
30. Peibst, R., Dürkop, T., Bugiel, E., Fissel, A., Costina, I., Hofmann, K.R.: Driving mechanisms for the formation of nanocrystals by annealing of ultrathin Ge layers in SiO_{2}. Phys. Rev. B **79**, 195316 (2009)
31. Zacharias, M., Streitenberger, P.: Crystallization of amorphous superlattices in the limit of ultrathin films with oxide interfaces. Phys. Rev. B **62**(12), 8391–8396 (2000)
32. Centurioni, E.: Generalized matrix method for calculation of internal light energy flux in mixed coherent and incoherent multilayers. Appl. Opt. **44**(35), 7532–7539 (2005), http://www.bo.imm.cnr.it/users/centurioni/optical.html
33. Allegrezza, M.: Minuitfit. http://www.bo.imm.cnr.it/users/allegrezza/minuit/minuitfit.html
34. Jellison Jr., G.E., Modine, F.A.: Parameterization of the optical functions of amorphous materials in the interband region. Appl. Phys. Lett. **69**(3), 371–373 (1996). Erratum, ibid. 69:2137
35. Jellison, G.E., Chisholm, M.F., Gorbatkin, S.M.: Optical functions of chemical vapor deposited thin-film silicon determined by spectroscopic ellipsometry. Appl. Phys. Lett. **62**(25), 3348–3350 (1993)
36. Aspnes, D.E., Studna, A.A.: Dielectric functions and optical parameters of Si, Ge, GaP, GaAs, GaSb, InP, InAs, and InSb from 1.5 to 6.0 eV. Phys. Rev. B **27**(2), 985–1009 (1983)
37. Palik, E.D.: Handbook of Optical Constants of Solids. Academic, New York, NY (1991)
38. Guerra, R., Degoli, E., Ossicini, S.: Size, oxidation, and strain in small Si/SiO$_2$ nanocrystals. Phys. Rev. B **80**(155332), 1–5 (2009)
39. Alonso, M.I., Marcus, I.C., Garriga, M., Goñi, A.R., Jedrzejewski, J., Balberg, I.: Evidence of quantum confinement effects on interband optical transitions in Si nanocrystals. Phys. Rev. B **82**(4), 045302 (2010)
40. Moreno, J.A., Garrido, B., Pellegrino, P., Garcia, C., Arbiol, J., Morante, J.R., Marie, P., Gourbilleau, F., Rizk, R.: Size dependence of refractive index of Si nanoclusters embedded in SiO2. J. Appl. Phys. **98**(1), 013523–013523-4 (2005)
41. Losurdo, M., Giangregorio, M.M., Capezzuto, P., Bruno, G., Cerqueira, M.F., Alves, E., Stepikhova, M.: Dielectric function of nanocrystalline silicon with few nanometers (<3 nm) grain size. Appl. Phys. Lett. **82**(18), 2993–2995 (2003)

42. Ding, L., Chen, T.P., Liu, Y., Ng, C.Y., Fung, S.: Optical properties of silicon nanocrystals embedded in a SiO_{2} matrix. Phys. Rev. B **72**, 125419 (2005)
43. Allegrezza, M., Hiller, D., Löper, P., Summonte, C.: Optical function and absorption edge of silicon nanocrystals, In: Proceedings of the E-MRS Spring Meeting, Strasbourg, France (2013)
44. Demontis, V., Sanna, C., Melskens, J., Santbergen, R., Smets, A.H.M., Damiano, A., Zeman, M.: The role of oxide interlayers in back reflector configurations for amorphous silicon solar cells. J. Appl. Phys. **113**(6), 064508–064508-9 (2013)
45. Dutta, U., Chatterjee, P.: The open circuit voltage in amorphous silicon p-i-n solar cells and its relationship to material, device and dark diode parameters. J. Appl. Phys. **96**(4), 2261–2271 (2004)
46. Hegedus, S.S.: Current–voltage analysis of a-Si and a-SiGe solar cells including voltage-dependent photocurrent collection. Prog. Photovolt. Res. Appl. **5**(3), 151–168 (1997)
47. Werner, J.H.: Schottky barrier and pn-junction I/V plots - small signal evaluation. Appl. Phys. A **47**, 291–300 (1988)
48. Crandall, R.S.: Modeling of thin film solar cells: uniform field approximation. J. Appl. Phys. **54**(12), 7176–7186 (1983)
49. Merten, J., Asensi, J.M., Voz, C., Shah, A.V., Platz, R., Andreu, J.: Improved equivalent circuit and analytical model for amorphous silicon solar cells and modules. IEEE Trans. Electron Dev. **45**(2), 423–429 (1998)